

# **Design of smart ISO liquid tank container - Full Mathematical Model, Simulation and Fabrication Proposal for FBG**

Calum Vermeulen

12 May 2025

# 1 Fiber Bragg Grating (FBG)

## 1.1 Introduction to the Fiber Bragg Grating Sensor

The constraints of tank design were influenced not only by ISO standards[1], but also by the tool used to convert the physical data to digital data. This conversion begins with the Fiber Bragg Grating in an optical fiber, where this grating is the essential changing property that is measured via an electronic sensor.

To adequately implement the design of the FBG based on simulation, the nature of forward and reflected light propagating through an optical fiber is mathematically modelled and decoupled. This communicates how external factors on the tank translate through different field effects into a measurable change in the central wavelength for a waveband of light.

Physical properties are measured by the changed grating; stress and strain induced on the tank and frame structure along with thermal expansion from the tank or surrounding area. These properties are crucially used to calculate the liquid level within the tank, while further monitoring the tank's structural health over a long-term period of use.

In industry settings, the liquid level in the tank is typically measured with something as simple as a dip stick. However, for corrosive, toxic, or contamination sensitive liquids, dip sticks[2] are unsuitable for measurement. As a result, industrial applications require non invasive methods such as FBG sensors mounted externally to the tank to measure the liquid level within.

Impressively, the FBG sensor presents a method of translating physical changes of tiny orders of magnitude into electrical values, and then digital values. Within an optical fiber, parallel gratings are purposefully inscribed onto the core of the fiber. These grating regions are spaced strategically throughout the body of the fiber, corresponding to a point of the structure being measured. These points experience deformation under strain and temperature changes, further deforming the grating of the fiber. These gratings reflect specific wavelengths of light, known as the Bragg Wavelength,  $\lambda_B$  back towards a measuring interrogator. This difference between the original central wavelength for the undeformed grating versus the new deformation influenced Bragg wavelength, is recorded as a shift in wavelength, where this shift is the quantity being measured to determine the strain on the tank.

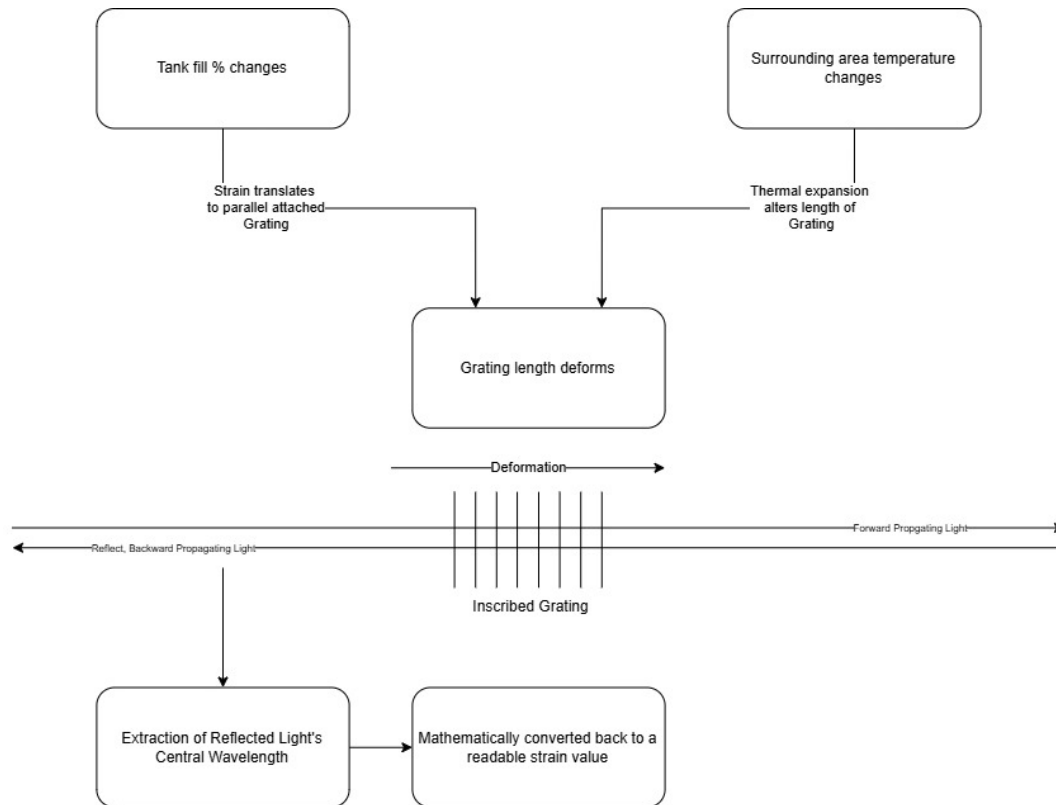


Figure 1: Illustration of an FBG sensing system, demonstrating the pipeline of how strain and thermal deformation lead to a readable digital measurement of strain.

Importantly, the FBG alone is only one part of the overall sensor system. While this section explores only the FBG, the following section on Spectroscopy?? completes the second half of the sensor, processing the physical changes of the grating into the electrical changes that can be digitized.

Additionally, the FBG is a powerful tool, being immune to electromagnetic fields and harsh field conditions, allowing it to survive conditions that other sensors would typically fail under. For only being external to the tank, these immunities are not essential; however, it is important to note for the viability of the sensor in other potential use cases. An example of an FBG being the immutable best in class sensing option is for an MRI[3], a device that by its nature generates an immense magnetic field with extreme electromagnetic interference, meaning that the FBG is ideal for monitoring strain or temperature, both within or in the surrounding area of the MRI. The sensor also has inherently strong multiplexing capabilities. Multiple sensing points can be inscribed along a single fiber without loss of signal integrity, provided that the interrogator and the bandwidth are sufficiently designed to separate the Bragg wavelength of each grating to avoid cross-talk, while implementing appropriate systems to handle multiple signals in place.

Since this project is entirely theoretical, the physical "design" and manufacture of the FBG only exists as a small section; including optical fiber selection, appropriate choice of adhesive, as well as inscribing of the grating on to the fiber core.

The obtained mathematical model represents the defining backbone of the simulation of the FBG, a design requirement to demonstrate the effective translation from physical qualities to digital quantities, and further used to implement the data processing post wavelength interrogation. The simulation utilises design constraints set by interrogation, the tank itself as well as relevant sources, and is then used to select the relevant optical fiber and FBG inscription technique.

The simulation is also essential in providing information to the FBG fabrication team, so that they can correctly alter the fiber core for correct light propagation in this application.

## 1.2 Mathematical Model - Principle of FBG Sensing

This section explores the mathematical representation of how the incoming optical signal is separated into its constituent forward and reflected propagation parts. This model describes how variations in physical parameters, such as strain and temperature, alter the central wavelength reflected by the grating. The final reflectivity profile obtained through the model can be enhanced using apodization, smoothing the spectral response and minimizing side lobes for clearer signal interpretation.

### 1.2.1 The Bragg Condition

The FBG consists of periodic refractive index variations within the core of an optical fiber that can be equated to a stop band filter, referred to as the Bragg grating, where only narrow optical fields are successfully reflected by the gratings to form coherent scattering along the index variations of a silica fiber. The strongest interaction between the light emission and gratings is referred to as the Bragg wavelength, and here forms a central peak in spectral reflectivity as seen in figure 3. The relationship between the Bragg wavelength and the Bragg grating is defined as the Bragg condition, which is mathematically defined as follows:

$$\lambda_B = 2n_{eff}\Lambda \quad (1)$$

Where:

- $\lambda_B$ : Bragg wavelength
- $n_{eff}$ : Effective refractive index
- $\Lambda$ : Grating Period

$n_{eff}$  defines the way that light propagates through a fiber, taking into account both core and the cladding that light can "leak" into. It can be understood as the ratio between the speed of light and the phase velocity of a guided wave in a fiber, described as:

$$n_{eff} = \frac{c}{c_{phase}} \quad (2)$$

It can be understood that the core of the fiber  $n_1$  has a different refractive index than that of the cladding  $n_2$ . Since light is not confined to just the core, the effective refractive index exists in between these values as:

$$n_2 < n_{eff} < n_1 \quad (3)$$

This means that in the Bragg condition1,  $n_{eff}$  defines the wavelength that is reflected by the grating of the FBG, where changes in the effective index come as a result of strain and thermal effects psychically compressing or stretching the fiber, changing the grating periodicity  $\Lambda$  and as such changing the Bragg wavelength  $\lambda_B$ [4]. Physically this is ensured by using a single mode fiber [5] with only one propagation mode, stabilising  $n_{eff}$  and avoiding modal dispersion for a clean narrow band reflectivity, increasing the precision of any strain and temperature measurements.

This shift in the Bragg wavelength is the basis for how an electrical system can measure the active strain induced on a structure, where the grating area of the fiber is attached to a surface, or a beam in the case of this project. The deformation of the beam will translate to the bound fiber optic cable, deforming the grating and shifting  $\lambda_B$ .

The specific relationship between the shifted Bragg wavelength and the strain on a structure is explored in sec 1.2.5.

### 1.2.2 Coupled Mode Theory and Wave Propagation

The propagation of light as  $n_{eff}$  in the fiber can be described using waveguide modes. These modes are separated by their interactions with the grating and, as such, diffract and reflect differently within the core of the fiber. The grating acts as a periodic perturbation that induces coupling between forward and backward propagating modes. For the effective analysis of the spectral profile of the deformed grating to occur, these coupled modes must be mathematically detangled, otherwise simulation to characterise the reflected spectral response is impossible, meaning there can be no determination of the Bragg wavelength shift and no strain measured.

To sufficiently decouple the forward and backward propagating modes, the diffraction of light induced via a periodic grating should be analysed[6]:

$$m\lambda = \Lambda(\sin\theta_i + \sin\theta_d) \quad (4)$$

Where:

- $m$ : Order of diffraction (integer)
- $\lambda$ : Wavelength
- $\Lambda$ : Grating Period
- $\theta_i, \theta_d$ : Angles of incidence and diffraction

This is visually expressed in figure 2.

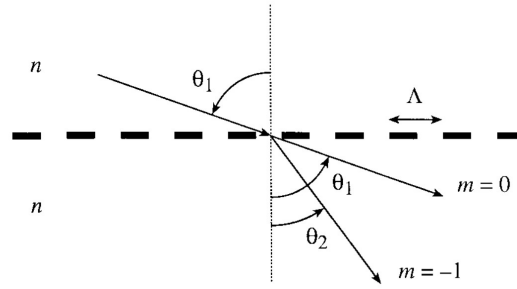


Figure 2: Grating induced diffraction orders of light [6]

To accurately simulate and interpret the spectral response of an FBG, it is essential to mathematically decouple the forward- and backward-propagating wave modes within the fiber. The periodic refractive index modulation caused by the grating induces coupling between these modes, redistributing energy in a wavelength-dependent manner. Without this decoupling, predicting reflectivity spectra and thus determining Bragg wavelength shifts becomes analytically intractable. This necessity leads directly to the application of Coupled Mode Theory (CMT)[7], a standard framework used to model mode interactions in weakly perturbed waveguides. CMT offers a means to represent how light exchanges between forward and backward directions as a function of position along the grating, ultimately yielding the reflectivity profile of the sensor[7]. It is not the goal of this report to derive CMT from first principles. Instead, we adopt the widely accepted formulation obtained from Maxwell's equations under the slowly-varying envelope approximation. This results in the pair of coupled differential equations 6 and 5 that describe the evolution of mode amplitudes along the grating, forming the mathematical basis for the FBG simulation model.

$$\frac{dA(z)}{dz} = jB(z)\kappa e^{j(\Delta\beta)z} \quad (5)$$

$$\frac{dB(z)}{dz} = jA(z)\kappa^* e^{j(\Delta\beta)z} \quad (6)$$

Where:

- $A(z), B(z)$  are the complex amplitudes of the forward and backward wavemodes
- $\kappa$  is the coupling coefficient 12
- $\Delta\beta$  is the detuning factor 11
- $z$  is the distance along grating, sometimes referred to as  $L$

For a general case, these complex modes  $A(z)$  and  $B(z)$  are described as the evolution of the wavemodes along the grating length, portrayed a complex differential. This standard form includes  $e^{j(\Delta\beta)z}$  as a phase term that explicitly represents spatial periodicity between the reflected Bragg wavelength and forward normal wavelength. This is mathematically complete but it adds numerical bloat to what can be a more simplified model, particularly for this design of uniform coupling and weak index modulation 2.4.1. To simplify for simulation preparation, the rotating wave approximation 2 can be adopted, effectively transforming the equations into a reference frame moving in parallel to the grating induced phase, thus eliminating the oscillatory phase term while maintaining accuracy under the weak coupling conditions 14 and slow envelope variation. This simplification refines the equations into the following:

$$\frac{dA(z)}{dz} = i\delta A(z) + i\kappa B(z) \quad (7)$$

$$\frac{dB(z)}{dz} = -i\delta B(z) - i\kappa^* A(z) \quad (8)$$

These complex amplitude differential equations now describe more simply how the wavemode or light interacts with a periodic refractive index perturbation in a FBG. These equations are governed by the following constants:

The propagation constant  $\beta$  characterises the axial phase evolution of the propagating light through the fiber core as:

$$\beta = \frac{2\pi n_{eff}}{\lambda} \quad (9)$$

$\lambda$  here is the forward propagating free wavelength in the fiber core. Where there is a grating, strong reflections comes when this propagation constant satisfies the Bragg condition 1 as defined by the Bragg propagation constant:

$$\beta_B = \frac{\pi}{\Lambda} \quad (10)$$

The detuning factor  $\delta$  represents the deviation of a wave from the Bragg resonance.

$$\delta = \beta - \beta_B = \frac{2\pi n_{eff}}{\lambda} - \frac{2\pi}{\Lambda} \quad (11)$$

When  $\delta = 0$ , the reflected and incident waves remain in phase across grating periods resulting in the largest reflection of the counter propagating wavemode. As  $\delta$  increase, the phase mismatch lowers the reflectivity and widens the spectral response, resulting in a waveform with thin peaks and wide bases, represented in figure 9 from the simulation as an example.

The strength of coupling between the counter propagating modes is governed by the coupling coefficient  $\kappa$  12; depending on the modulation depth of the refractive index and the overlap of the mode field with the grating:

$$\kappa(z) = \frac{\pi \Delta n}{\lambda} \cdot \eta \quad (12)$$

Where  $\Delta n$  is the amplitude of the index modulation and  $\eta$  is the mode overlap integral, an efficiency factor to approximate the normalised mode overlap integral, useful for simplified expressions of the coupling coefficient for simulation purposes.

Otherwise, the coupling coefficient can be more formally recognised including the mode overlap integral [8] as:

$$\kappa = \int_{-\infty}^{+\infty} \int_{-\infty}^{+\infty} \frac{\Delta n}{2} \xi_{vt} \xi_{vt}^* dx dy \quad (13)$$

In this context, adopting the approximate form using  $\eta$  is justified, as the fiber structure is weakly guiding and the wavemodes are symmetric. These conditions allow the simplified expression for  $\kappa$  to serve as a reliable and computationally efficient substitute.

This system can be assumed as weakly coupled, which is a standard approximation of CMT where the coupling coefficient  $\kappa$  is much smaller than the propagation constant  $\beta$  of the unperturbed wave mode.

$$\left| \frac{\kappa}{\beta} \right| \ll 1 \quad (14)$$

Satisfying this condition ensures the wavemode amplitudes  $A(z)$  and  $B(z)$  evolve slowly along their respective propagation direction, resulting in coupling occurring over a length scale much greater than the wavelength of the light emission. When this condition is met, the phase term  $e^{j\Delta\beta z}$  can be effectively neglected, allowing for the simplified terms in equations 7 and 8. This approach aligns with methods established in literature [6].

### 1.2.3 Transfer Matrix Method (TMM)

While the simplified CMT equations 7 and 8 capture the underlying physics of wavemode coupling in optical fibers as a result of an FBG, analytical mathematics is not always practical for deriving a reflectivity spectra. To reduce complexity, the transfer matrix method[9] (TMM) is employed, used to discretise the grating into small segments, modeling the light propagating through each segment as a matrix operation. TMM offers an efficient and numerically sound approach to form the primary method of simulating a full reflectivity spectrum across a wide range of wavelengths and grating profiles.

More specifically, to solve the coupled mode equations numerically, the length  $L$  of the grating must be divided into  $N$  number of uniform sections as  $\Delta(z)$ , with each segment treated as containing a set of constant parameters, resulting in  $\Delta(z) = \frac{L}{N}$ . Within each segment,  $\Delta n$  is assumed to be constant to justify the use of a local transfer matrix as the model for the counter propagating wave modes amplitudes and their evolution through the core:

$$\begin{bmatrix} A(z + \Delta z) \\ B(z + \Delta z) \end{bmatrix} = T(\Delta z) \begin{bmatrix} A(z) \\ B(z) \end{bmatrix} \quad (15)$$

Where  $T(\Delta z)$ , or  $T_i$ , can be taken as the coupled mode equations in the form:

$$T(i) = \begin{bmatrix} \cosh(\gamma_i \Delta z) - i \frac{\delta_i}{\gamma_i} \sinh(\gamma_i \Delta z) & \frac{i \kappa_i}{\gamma_i} \sinh(\gamma_i \Delta z) \\ -\frac{i \kappa_i^*}{\gamma_i} \sinh(\gamma_i \Delta z) & \cosh(\gamma_i \Delta z) + i \frac{\delta_i}{\gamma_i} \sinh(\gamma_i \Delta z) \end{bmatrix} \quad (16)$$

Where:

- $\kappa_i$  is the local coupling coefficient in segment  $i$
- $\delta_i$  is the detuning factor for that segment
- $\gamma_i = \sqrt{|\kappa_i|^2 - \delta_i^2}$  is the complex propagation constant under weakly modulated conditions

The global response of the grating is the product of all locally derived transfer function segment matrices in order:

$$T = T_N T_{N-1} \dots T_1 \quad (17)$$

Or written differently as

$$T_{GLOBAL} = \prod_{i=1}^N T_i \quad (18)$$

The global transfer matrix  $T$  is the relationship between the input and output mode amplitudes across the full length  $\Delta z$  of the grating. Under the assumption that the fiber is terminated where  $z = L$ , or where as a result of no counter propagating light such that  $B(L) = 0$ , the following boundary condition can be applied:

$$\begin{bmatrix} A(L) \\ B(L) \end{bmatrix} = T_{GLOBAL} \begin{bmatrix} A(0) \\ 0 \end{bmatrix} \quad (19)$$

Solving for  $\frac{B(0)}{A(0)}$  yields the complex reflectivity of the grating as  $r$ . Thus, the power reflectivity is then:

$$R = \left| \frac{B(0)}{A(0)} \right|^2 = |r|^2 \quad (20)$$

The modular treatment that TMM uses for modeling finer sections of the grating, alongside its numerical stability under both weak and strong coupling conditions and its compatibility with variable grating profiles makes it an excellent analytical method for accurately simulating an FBG to aid in a sensor system design.

#### 1.2.4 Apodization

In an FBG, sudden gain and loss in refractive index modulation results in unnecessary side lobes in the reflection spectrum. These sharp spectral output side lobes come from the grating period discontinuing which leads to energy leaking outside of the main lobe within the Fourier domain.

To suppress these spectral lobes at a small cost to spectral reflectivity of the grating, an apodization profile is applied into the TMM. It is a process by which modulation amplitude of the refractive index is gradually tapered along the grating length.

Within the TMM, apodization can be implemented by modifying the coupling coefficient<sup>12</sup>  $\kappa(z)$ , which is directly proportional to the local modulation amplitude  $\Delta n(z)$ . In a uniform grating,  $\kappa(z) = \kappa_0$  is constant, whereas in an apodized grating,  $\kappa(z)$  varies smoothly with position.

Apodization is commonly applied via a Gaussian profile<sup>[8]</sup>:

$$\kappa(z) = \kappa_0 \times e^{\left[ -\left( \frac{z - \frac{L}{2}}{\sigma} \right)^2 \right]} \quad (21)$$

Where:

- $L$  is the total grating length
- $\sigma$  is the width of the Gaussian envelope
- $\kappa_0$  is the peak coupling coefficient at the center of the grating

To implement this into the TMM, apodization needs be used to modify the coupling coefficient  $\kappa_i$  for each segment. Where  $f(z_i)$  is the chosen apodization function and  $z_i = i \times \Delta z$  is the position of the  $i^{th}$  segment, this can form a product with the coupling coefficient as:

$$\kappa_i = \kappa_0 \times f(z_i) \quad (22)$$

This product propagates directly through the local transfer matrix  $T_i$  for each segment, subtly adjusting the reflectivity as a function of wavelength.



To aid in visual understanding of the final reflectivity spectrum after complete decoupling via CMT and modeling of each segment via TMM, an apodized and unapodized plot in figures 3 and 4 can be demonstrated to suggest completion of the mathematical model.

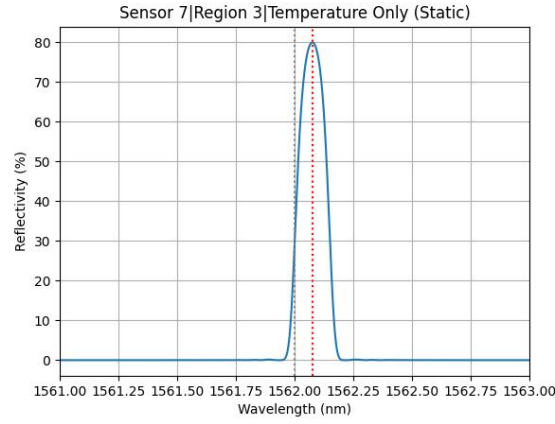


Figure 3: Apodized reflectivity spectrum, with a reflectivity of 80% but only one clear peak.

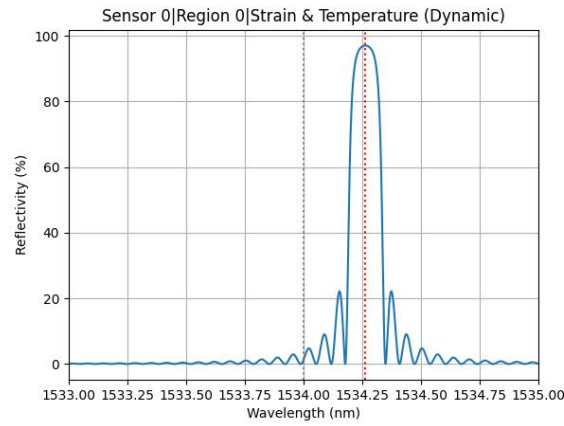


Figure 4: Unapodized reflectivity spectrum, higher reflectivity of 96% but with extensive side lobes.

\*\*Note to reader, figures 3 and 4 are both operating over different central wavelengths and Bragg wavelengths. This is not indicative of any different modeling design options, this simply comes as a result of two different sensors operating on their own central wavelengths being chosen. Additionally, as explained in the simulation section 2, random mass values are used each run of the simulation, resulting in different Bragg wavelength shifts, as seen above, where the apodized and unapodized figures come from two different simulations.

### 1.2.5 Incorporating Mechanical and Thermal Effects

Now that the primary behaviour of light in the fiber has been modeled, it needs to be appropriately manipulated to correctly produce the shifted central Bragg wavelength, created as a result of the grating deformation.

Fortunately, the FBG is highly sensitive to minor changes in strain or temperature and can be tuned appropriately. Although the later steps of the model remain true for the deformed FBG, the relationship that alters the grating periodicity needs to be explored and updated in the model to determine the shifted central wavelength.

The change in Bragg wavelength and thus grating periodicity due to induced mechanical strain ( $\epsilon$ ) and temperature change ( $\Delta T$ ) is mathematically expressed as follows:

$$\Delta\lambda_B = \lambda_B [(1 - \rho_e)\epsilon + \alpha_T \Delta T] \quad (23)$$

Where:

- $\Delta\lambda_B$  is the resulting shift in Bragg wavelength
- $\epsilon$  is the applied mechanical strain due to a change in the liquid fill of the tank
- $\rho_e = \frac{n_{eff}^2}{2}(\rho_{12} - v(\rho_{11} + \rho_{12}))$  is the effective photoelastic coefficient [10]
- $\alpha_T$  is the thermo-optic coefficient
- $\Delta T$  is the measured change in temperature

The thermo-optic coefficient  $\alpha$  1.2.5 encapsulates both material expansion  $\zeta$  and refractive index variation  $\beta_T$  due to temperature. For modeling and simulation:

$$\alpha = \zeta + \beta_T \quad (24)$$

Where,

- $\zeta$  is the thermo optic coefficient, accounting for changes in the refractive index due to temperature
- $\beta_T$  is the thermal expansion coefficient, describing the changes in the grating period due to thermal dilation.

Deriving these components from first principles aids in defining how the shifted Bragg wavelength in the FBG can be used to determine the strain deforming a structure, or the thermal effects incident on that structure. Thus, these coefficients are described as:

$$\beta = \frac{1}{\Lambda} \times \frac{d\Lambda}{dT} \quad (25)$$

and

$$\zeta = \frac{1}{n_{eff}} \times \frac{dn_{eff}}{dT} \quad (26)$$

Equation 23 and the following equations[11] explicitly links mechanical deformation, as strain, as well as temperature changes to measurable shifts of the central Bragg wavelength, allowing for direct interpretation of physical conditions from optical measurements. If a sensor measures only the strain, then  $\Delta T$  can be set to 0, and vice versa if the strain is not required in the calculation.

Importantly, this shifted Bragg wavelength is in direct relationship to a different grating periodicity. This means that the shifted wavelength can be explicitly used in the transfer matrix for complete simulation of a deformed Bragg grating. This highlights the incredible strength of the FBG sensor, a physical change in the structure leads to a physical change in the grating, leading to a measurable change in the optical signal transmitted to the interrogator. All while requiring no changes to the modeling of the light in the fiber or at the sensor itself.

## 2 Simulation of Fiber Bragg Grating (FBG)

The goal of this project is to create a production-ready design that can be used by any on site engineer to read the current liquid height within the tank, as well as to monitor the structural health of the specific tank over prolonged periods of time. To enable this end-user experience, the FBG sensor needs to be simulated using all of the above modeling defined in the previous section 1.2, while being specific to the tank, fiber, and spectroscopy conditions of this project.

Each of these physical properties are sufficiently selected by robust research or by specific requirements defined by the team. For example, obtaining a high reflectivity % with a moderate spectral bandwidth was essential for the spectroscopy team, or factors such as refractive index modulation and apodization being tuned in accordance with the required sensitivity of the FBG, which is directly influenced by the strain experienced on the beam. If the beam experiences a low strain across its structure, then a thinner spectral peak would be required to more accurately locate the new shifted Bragg wavelength in interrogation. Simulation is essential to ensure that the tank design is translated effectively to digital data for user reading and structural health monitoring.

In methodology, the implementation of the simulation must appropriately reflect how the grating within the core of the fiber is altered by the liquid-induced strain of the tank, as well as the surrounding temperature, measured by a separate FBG, detached from the frame structure but in the exact same region (beam). The further use of this affected grating and Bragg wavelength then influences the reflected light obtained by the transfer matrix method, where the shifted Bragg wavelength is obtained by equation 23. The simulation cannot end with just obtaining a spectral peak; it must also be able to translate the reflected light back into a readable strain, using equation 23 to decouple the temperature and strain on the FBG to solely read the stress on a particular selected region.

The strain needs to be converted back to a liquid fill % by using the relationship 27 determined in section ??, between fill volume and strain. For simulation purposes, this relationship was better defined as a dynamic lookup table, where a baseline tank strain and a liquid mass would be used to define the maximum and minimum strain that could be incident on the tank for a particular liquid type. The type of liquid is essential, as the system relies on an input of liquid density for correct calculation of liquid mass used and available mass in the tank. This method allowed recovered strains, after the TMM, to be mapped back to the lookup table to acquire the corresponding liquid fill percentage. While FEA analysis originally informed these relationships, it was later replaced with a simulation based lookup table due to time and resolution constraints. Finally, the fill volume is converted to a liquid height within the tank by inverting the circle segment area equation shown below in equation 34.

## 2.1 Simulation Setup

Focusing on the simulation individually, and not the full GUI, the simulation is built in a Python workspace, with a work flow as follows in figure 5.

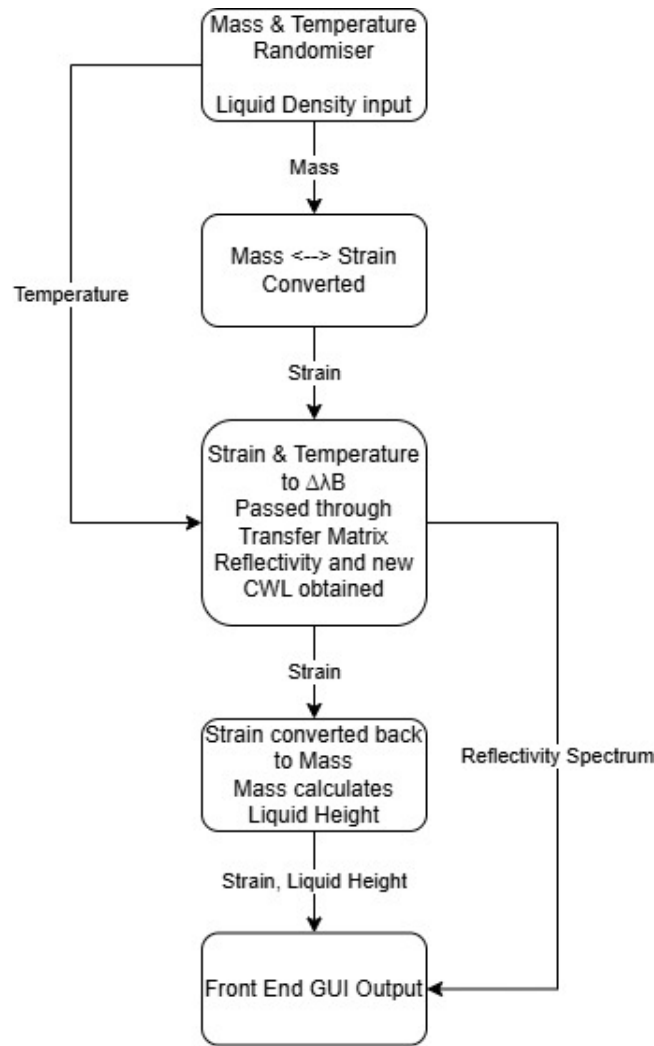


Figure 5: Flow chart for simulation of FBG

This workflow will be expanded upon in the given these sections 2.2??.

## 2.2 Determining Mass and Temperature for Simulation

A random mass and temperature generator was implemented for simplicity. With the project being theoretical, there is no live tank to measure, and as such it is more efficient to generate a mass value greater than 80%, which is prescribed as the minimum tank fill in section ?? fill and a temperature value between  $-40^{\circ}\text{C}$  and  $+130^{\circ}\text{C}$ ?. In earlier versions of the simulation, strain values from the FEA simulation were used to test the accuracy of the FBG. However, once a relationship was created in the form of a lookup table, random values could be selected from the table and used for simulation.

Implementing this random generator made testing under different environment profiles seamless, borderline operating as a quicker simulator of strain at a region depending on volume of liquid and liquid density than the finite element analysis, which suffered from time consuming simulation of the tank and frame as a whole. With this method, particular liquids can now be measured instantly for the strain they induce on the beam, allowing for easy selection of liquids that the tank can handle. For example, mercury has a liquid density 13 times greater than that of water, leading to a beam strain of  $1.823 \times 10^{-3}$  at 81% fill volume according to the FBG simulation. Since 80% volume is the minimum tank fill, this high strain is out of scope for this tank and will lead to rapid failure in the frame structure. This FBG simulation as such can supplement extensive FEA simulation for obvious outlying liquid types.

## 2.3 Relationship Between Mass and Strain

The randomised mass is then used to calculate the strain of the tank beam under the particular conditions. The liquid mass is modeled as a uniformly distributed load on a simply supported beam that acts as the tank strut as discussed in section ??, where equation 27 is explicitly used to determine the strain on deforming the grating in the FBG as a result of liquid mass in the tank.

$$\epsilon = \frac{mgLy}{8EI} \quad (27)$$

Conversely, the equation is rearranged as equation 28 to re-obtain the liquid mass in the tank, as the strain is being realistically translated through an FBG to obtain the liquid height in the tank, which the liquid mass is required to calculate.

$$m = \frac{8\epsilon EI}{gLy} \quad (28)$$

This inverse relationship will directly enable the FBG simulation to determine the liquid height within the tank.

## 2.4 Transfer Matrix Method

The simulation relies on the Transfer Matrix Method (TMM) outlined in sec 1.2.3 to interpret the reflectivity spectra of the shifted central Bragg wavelength by iterating over a number of defined segments, all done at once via vectorization of the transfer matrix loop.

### 2.4.1 Simulation Parametres

The FBG spectra response simulation uses a range of constants and coefficients, typically derived from industry standards and optical fiber datasheets, as well as information on the tank design from the mechanical team. Parametres include:

- Grating Length = 200 mm
- $n_{eff} = 1.45$ : Effective Refractive Index
- $\lambda_B = 1550nm$ : Base Bragg Wavelength
- $\Delta n_{eff} = 1 \times 10^{-4}$ : Effective Refractive Index Modulation
- Fringe Visibility Factor = 1
- Photoelastic coefficients;  $p_{11} = 0.121$  &  $p_{12} = 0.27$  [10]
- $p_\epsilon = 0.22$ : Photoelastic Constant
- $\nu = 0.17$ : Poisson's Ratio [10]
- $\alpha_T = 8.6 \times 10^{-6}^\circ C^{-1}$ : Thermo-optic coefficient [12]
- Insertion Loss: 0.2 dB/m

### 2.4.2 Vectorized Transfer Matrix

Implementation of the transfer matrix method discussed in section 1.2.3 is used to find the wavelength dependent reflectivity spectrum of an FBG sensor over a particular Bragg wavelength. This implementation is designed for speed and scalability, using vectorization to allow for an incredibly fast evaluation of how the FBG reflects different wavelengths of light. As the mathematics of how the TMM is implemented has already been explored, this section will focus on the numerical implementation from a software perspective and follows the workflow shown in figure 6.

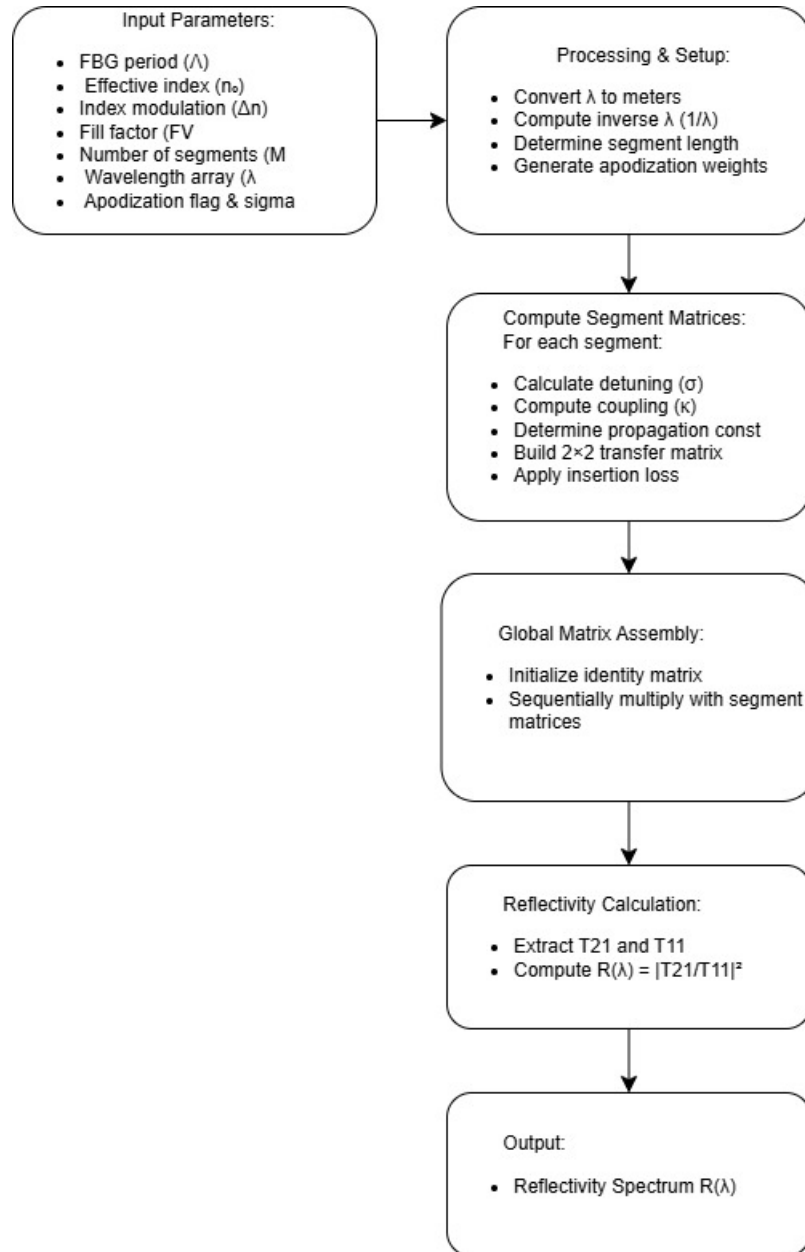


Figure 6: Transfer Matrix Method Simulation

The function is vectorized, meaning that it operates on entire arrays of wavelengths at once rather than simulating each array individually. The Python library NumPy [13] used for scientific computing is used for this, allowing fast, memory-efficient operations on arrays. It significantly sped up this simulation, when adding many FBG's with high reflectivities, simulation time would take up to a handful of minutes. Vectorization reduced the simulation time to barely a few seconds while maintaining physical accuracy.

The function begins by converting a list of wavelengths to metres, with arrays constructed to hold interte results, housing wavelengths compared to each grating segment as a  $M \times N$  shape.

The detuning term in equation 11 and the coupling coefficient 12 are computed for each segment and wavelength. These physical equations take into account apodization described in sec1.2.4, increase the smoothness of the reflectivity spectrum, removing side lobes at the cost of some reflectivity.

A propagation constant in equation 9 uses a complex-valued term  $\gamma$  derived for each pair  $M \times N$ , determining how much line is reflected and transmitted. The function relies on `np.where`, acting as a vectorized "if" statement, deciding whether the value should be real or imaginary depending on the sign of the interry term.

Each segment is represented by a  $2 \times 2$  matrix that manages how light behaves while moving through

the segment. The segments are sequentially multiplied together using NumPy's `einsum` function, thus performing tensor contractions, which are far faster and more flexible for multidimensional arrays as opposed to regular matrix multiplication.

Insertion loss is as an exponential decay to account for the signal loss experienced as light passes through each segment. See section 2.7 for more on insertion loss.

Finally, the reflectivity is obtained as a percentage by combining each segment matrix into one large global matrix, with the reflectivity obtained from specific matrix elements as shown in equation 20. Once again, vectorization enables all wavelengths to be rapidly computed at once, producing a 1D array of reflected power values. This array of  $R(\lambda)$  represents how strongly the FBG reflects each wavelength of light. When outputted to a plot, the highest and sharpest peak are indicative of the central Bragg wavelength for that FBG under the simulated conditions.

## 2.5 Undeformed vs. Deformed Conditions

The simulation pipeline is split into the evaluation of three distinct physical states, primarily an FBG being subject to just thermal conditions, and one subject to both strain and thermal conditions. These must be defined separately so that the shared strain and thermal effects on one FBG can be decoupled to obtain a strain exclusive measurement. The three physical states are described in more detail as:

- **Undeformed Condition:** This baseline scenario considers no external strain or thermal variation. The resulting reflectivity profile represents the initial central wavelength and baseline reflectivity.
- **Thermal Only Condition:** Reflectivity profiles are simulated by applying temperature changes without mechanical strain, highlighting shifts in central wavelength due solely to thermal expansions and refractive index variation.
- **Combined Strain and Temperature Conditions:** Reflectivity simulations incorporate both mechanical strain and temperature changes, showcasing combined effects on the central wavelength shifts. This provides insights into real world operational conditions.

The strain and temperature equation 23 in section 1.2.5 is highly relevant for this section. Each of these conditions are simulated by taking a sensor's central Bragg wavelength, an input strain  $\epsilon$ , and a temperature shift  $\Delta T$  to produce a high resolution reflectivity spectrum over a small  $\pm 1nm$  window range.

### 2.5.1 Undeformed Condition

Used in earlier versions of the simulation as it was being built, the undeformed case represents the sensors initial state, under zero liquid induced strain (only tank body and frame induced strain) and no temperature variation. This state was important in establishing a fixed base CWL for the sensor to operate from, allowing ease of interpretation of shifts in the reflectivity spectra as caused by environmental conditions.

Simplifying equation 23 to obtain an equation that does not represent strain or thermal effects. The unchanged grating period is defined as follows:

$$\Lambda_0 = \frac{\lambda_B}{2n_0} \quad (29)$$

### 2.5.2 Thermal-Only Deformation

The purpose of having a thermal only sensor is expanded in 2.5.4. For now, obtaining the thermal-only deformation is isolated using only the thermo-optic coefficient 2.4.1  $\alpha$  to determine  $\Lambda_T$  as:

$$\Lambda_T = \frac{\lambda_B(1 + \alpha\Delta T)}{2n_0} \quad (30)$$

Here, the refractive index remains fixed, but the effective Bragg wavelength shifts due to the expansion of the grating structure and temperature induced refractive index changes.

Furthermore, since the FBG never measures the true temperature and only measures the temperature from a common reference temperature for all sensors, this common temperature must be defined, which in this simulation is set to  $20^\circ C$ .

### 2.5.3 Combined Strain and Temperature Deformation

In the final condition, both strain and temperature deformation variations experienced by the sensor are mathematically applied simultaneously. Resulting in the final grating period being defined as a rearranged version of equation 23 as:

$$\Lambda_D = \frac{\lambda_B[1 + (1 - p_e)\epsilon + \alpha\Delta T]}{2n_0} \quad (31)$$

### 2.5.4 Decoupling Strain and Temperature

Although the combined strain and temperature effectively capture the world dynamic changes that a single sensor will experience, this sensor will not be able to accurately determine the strain at a particular region on the beam as it is also experiencing thermal deformation. Thus, a temperature only sensor is added as close to the combined conditions sensor. This sensor, specifically where the grating is located, is left unbound to the structure, meaning that it will not expand or shrink along the beam as liquid is filled into the tank. However, this FBG sensor will still experience thermal changes at the same rate as the combined sensor. Recording both sensors for a specific region is essential for decoupling the effects of both strain and temperature on the combined condition sensor. To isolate the effects of just strain on the combined sensor, the temperature is removed via a reworking of the above equations in section 1.2.5.

The simulation establishes a temperature only sensor as static, setting  $\epsilon = 0$ , while a strain sensitive sensor is considered as dynamic, with both thermal and strain effects being incident on it.

Let:

- $\lambda_T$  is the observed peak from the static sensor
- $\lambda_D$  is the observed peak from the dynamic sensor
- $\lambda_{0,T}, \lambda_{0,D}$  is the known undeformed Bragg wavelength for both sensors

In the simulation, these dynamic and static sensors are grouped according to regions, marking each beam with an explicit temperature and strain sensitive sensor, as well as thermal only sensor. This pairing enables the system to implement the following decoupling methodology.

Thus, the static sensor at  $\epsilon = 0$  is:

$$\frac{\lambda_T}{\lambda_{0T}} - 1 = \alpha\Delta T \implies \Delta T = \frac{\frac{\lambda_T}{\lambda_{0T}} - 1}{\alpha} \quad (32)$$

And, substituting  $\Delta T$  into the dynamic sensor location (strain and temperature), it can be rearranged to solve for strain  $\epsilon$  as:

$$\epsilon = \frac{(\frac{\lambda_D}{\lambda_{0D}} - 1) - \alpha\Delta T}{1 - p_e} \quad (33)$$

This now considers the effects of strain and temperature on the dynamic sensor to be decoupled, with only the recorded strain of the tank being recorded and sent to the user.

## 2.6 Conversion from Liquid Height to Volume

Once the strain has been decouple from temperature as demonstrated in section 2.5.4 and has been extracted from the reflectivity spectrum in section 2.4, that strain is mapped to an internal liquid mass using the calibrated lookup table influenced by the FEA assumptions. This mass is simply converted to a liquid fill volume as a product of the chosen liquid density.

To determine the correct liquid height within the tank, the simulation inverts the standard circular segment equation for a horizontal cylinder tank [14]. Rather than directly measuring height, the model numerically solves for the height  $h$  that would produce the known volume using:



$$A = r^2 \cos^{-1} \left( \frac{r-h}{r} \right) - (r-h) \sqrt{2rh - h^2} \quad (34)$$

$$V(h) = A(h) \times L \quad (35)$$

- $R$  is the tank's internal radius ??
- $L$  is the tank's length ??
- $A(h)$  is the cross sectional area of the filled segment

This inversion is performed using the bisection method, enabling a numerical solution for  $h$  from any valid estimate. In cases where the circular segment inversion fails, for example as a result of ill conditioned inputs, the simulation falls back to a simplified cylindrical approximation:

## 2.7 Reflectivity and Bandwidth Calculation

Reflectivity profiles yield the essential metrics required by the spectroscopy team for interrogation of the central wavelength. These metrics include:

- Reflectivity (%): Peak reflectivity under various conditions of undeformed, thermal only deformation, and full strain deformation.
- 3 dB Bandwidth or full width half modulation (FWHM): Spectral width measured at half-maximum reflectivity, indicative of sensor resolution and performance.

The insertion loss in  $Np/m$  and bandwidth offer two critical parameters with strong influence on the effectiveness of the FBG sensor systems, specifically related to both spectroscopy and the fabrication inscription phase of the fiber optic cable. Insertion loss is the amount of optical power (dB) lost by interference with the fiber grating[15]. For spectroscopy, it is essential to minimise this insertion loss to ensure that the reflected light signal retains enough strength at the interrogator. Multiplexing the fiber further accentuates this need, as multiple gratings will result in even more signal loss by the time the signal reaches the interrogator. Significant insertion loss results in poor signal:noise ratios[16], further reducing the accuracy of wavelength detection, leading to inaccurate strain measurements.

Bandwidth is measured as the full width at half maximum (FWHM) of the reflected spectrum, commonly referred to as 3dB, with FWHM values in sensing systems typically ranging from 0.05 nm to 0.3 nm  $nm$ [15], with a high dependency on grating length and index modulation. For spectroscopy, a narrower bandwidth implies higher wavelength selectivity, enhancing the resolution of the light received at the interrogator and allowing for finer filtering between closely spaced sensors. For this design, the Bragg wavelength for each grating is separated by 4  $nm$ , a significantly large window to avoid cross-talk as visually represented in figure 8. Thus, a short bandwidth did not act as an extreme design constraint for this simulation, but was still taken into account. This extreme separation of Bragg wavelengths, in fact further supports this sensing system design, since a narrower bandwidth leads to the system having a higher susceptibility to noise, wavelength drifts, and environmental perturbations, and this tank requires eight FBG's along a fiber wrapped around a tank for transporting moving liquids, and standard bandwidth of 3 dB is clearly the most acceptable choice. Conversely, an excessively large bandwidth means the interrogator will have a harder time determining the peak central wavelength, leading to poor quality of information read by the interrogator.

Furthermore, the required bandwidth is an essential physical aspect of the FBG inscription. FBG fabrication, further talked about in section 4, in any of its forms (phase masks, point-by-point femtosecond lasers, and interferometric methods) requires incredibly high levels of precision for inscribing each sensor's grating profiles. Excessive insertion loss during inscription implies scattering or absorption defects within the fiber, which can have an effect on the long-term health and reliability [17] of the sensor. Moreover, control of the bandwidth is tied to the physical length of the grating at that region in the fiber, as well as the index modulation depth of the fiber as a whole. Through simulation, the optimal values for the bandwidth and  $\Delta N$  were determined to ensure that each grating behaves as designed for its targeted spectral range.

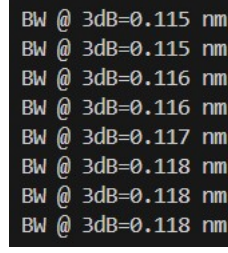


Figure 7: Bandwidth of designed FBG at 3 dB

Reflectivity, defined by equation 20, can be states as the fraction of incident optical power that is reflected by the grating at wavelength  $\lambda$ . Physically,  $R$  is governed by the grating's coupling coefficient 12, the grating length  $L$  and any apodization profile (50 in this simulation). A stronger refractive index modulation  $\Delta n_{eff}$  2.4.1 or longer  $L$  both raise the peak reflectivity, while apodization shapes the spectral envelope and suppresses side lobes.

In spectroscopy, for sufficient interrogation a high peak reflectivity is essential because it directly sets the amplitude of the returned signal at the interrogator. A larger  $R$  imposes the signal-to-noise ratio, making central wavelength shifts easier to resolve, especially when multiple sensors are multiplexed alone one fiber. At the same time, control of the reflectivity bandwidth, via detuning and apodization, ensures that the individual gratings remain spectrally unique, preventing cross talk and enabling finer discrimination between closely spaced sensors.

## 2.8 Bragg Wavelength Separation Strategy

Briefly mentioned in the above section, this design simulation used a Bragg wavelength separation of  $4nm$ . This is taken as a design consideration to allow multiplexed interrogation of multiple FBG sensors along a single fiber optic cable, where each sensor is assigned a unique central Bragg wavelength, and thus a unique grating periodicity according to the Bragg condition 1. The separation of  $4nm$  is chosen as a specific balance of spectral isolation and total sensor capacity. Given the FBG 2 dB bandwidth of  $0.117nm$ , this separation ensures minimal cross talk, even under extreme mechanical strain or thermal shifts, while maintaining simple peak detection in the reflectivity spectrum.

The number of independent FBG's that require isolated regions along the cable is defined by the mechanical need for structural health monitoring as well as determining the liquid height in the tank. As discussed previously, two sensors are needed per region to decouple mechanical strain and thermal effects in a particular region. These regions are set as four beams carrying a uniform load from the tank. Thus, eight sensors are required over some range of the source broadband input into the optical fiber.

The bandwidth of the broadband light source used in the system is defined by the spectroscopy selected superluminescent diode (SLD) in section ??, operating in an emission range of  $40nm$ , from  $1530nm$  to  $1570nm$ . This means that within this  $40nm$  range, an effective separation that allows for eight sensors without the possibility of cross talk is concluded as  $4nm$ .

Table 1: Central Bragg Wavelength Allocation for 8-Sensor FBG Array

Beam	1		2		3		4	
Sensor Index	1	2	3	4	5	6	7	8
Strain + Temp (nm)	1534	-	1542	-	1550	-	1558	-
Temp Only (nm)	-	1538	-	1546	-	1554	-	1562

## 3 FBG Simulation Results and Implementation Pathway

This section begins by presenting the simulated results of the FBG simulation in its final complete form. Presenting an accurate reflectivity spectrum over a deformed length of grating, showing a complete understanding of the core principles of an FBG sensor. This is then extended into a further section which, from a firmware perspective, presents how to tie this mathematical simulation into a real world implementation for an FBG sensor.

### 3.1 Simulation results

The simulation generates a full digital pipeline of the FBG system, from applied liquid load and temperature changes to the final reflectivity spectra and derived physical qualities. For modeling eight FBG sensors over four beam regions, with each region sharing a twin pair of sensors, one measuring both mechanical strain and thermal effects and one handling just thermal effects, all along one optical fiber cable, the following simulation outputs were obtained.

For each sensor, the reflectivity was simulated in a  $\pm 1nm$  window around its assigned Bragg wavelength 1. These spectra are shaped by temperature and/or strain, allowing the central Bragg wavelength shifts to be visually and numerically evaluated.

#### 3.1.1 All 8 FBG's Sensors Across One Broadband Signal

Figure 8 is used to demonstrate the wide separation between each of the eight sensors within the SLD defined range of  $40nm$ . Given the tiny shifts shown in the figures representing each individual FBG in the following sections, it is clear that this separation is very sufficient and that the spectroscopy team will be able to easily identify each sensor.

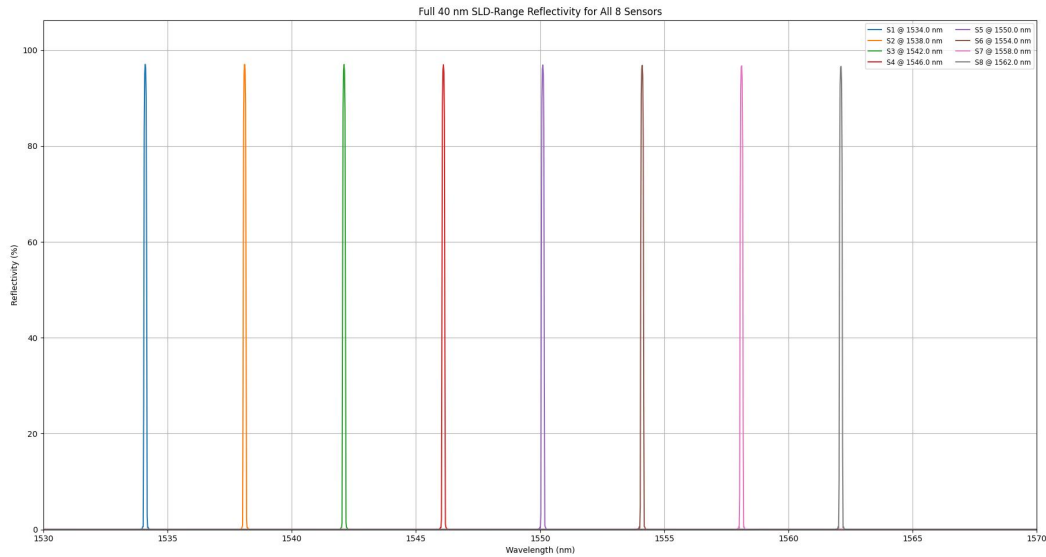


Figure 8: All eight FBG sensors reflectivity spectrum's modeled along one single fiber optic cable, showing their  $4nm$  separation to avoid cross talk

The following figures 9 and 10 highlight the full reflectivity spectrum of each FBG as it is marginally shifted from its original central wavelength to each FBG's new respective Bragg wavelength. Each group of FBG's are paired in their respective segments, with in depth summaries for the reflectivity of each sensor as well as other FBG factors included in section 3.1.3.

### 3.1.2 Beam 1 Sensor Pair

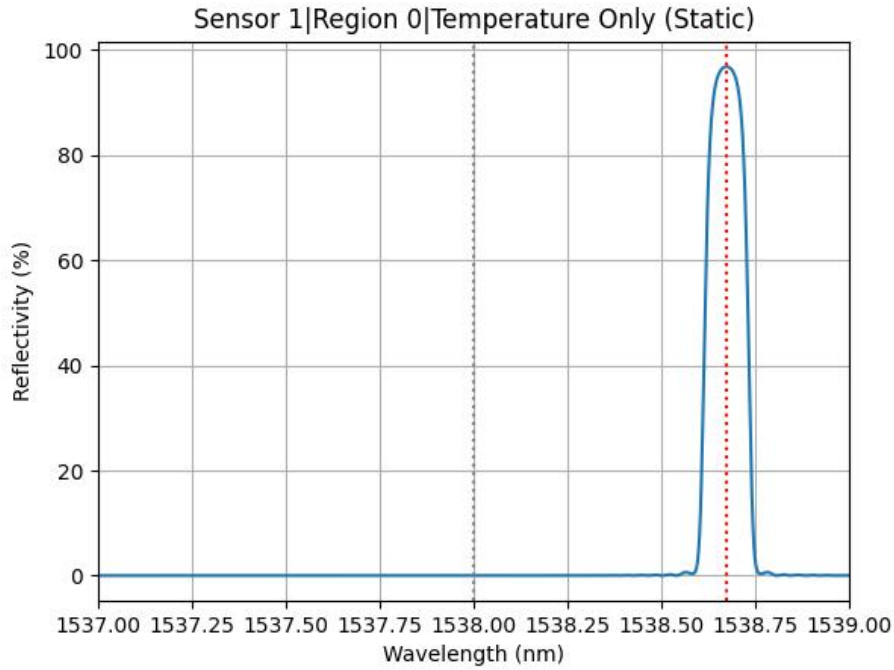


Figure 9: Temperature only sensor on region 0, or beam 1. The sensor is operating around a CWL of  $1534\text{nm}$ , and is shifted along the axis by a randomised liquid mass of  $16986.52\text{kg}$  at a temperature of  $42.89^\circ\text{C}$

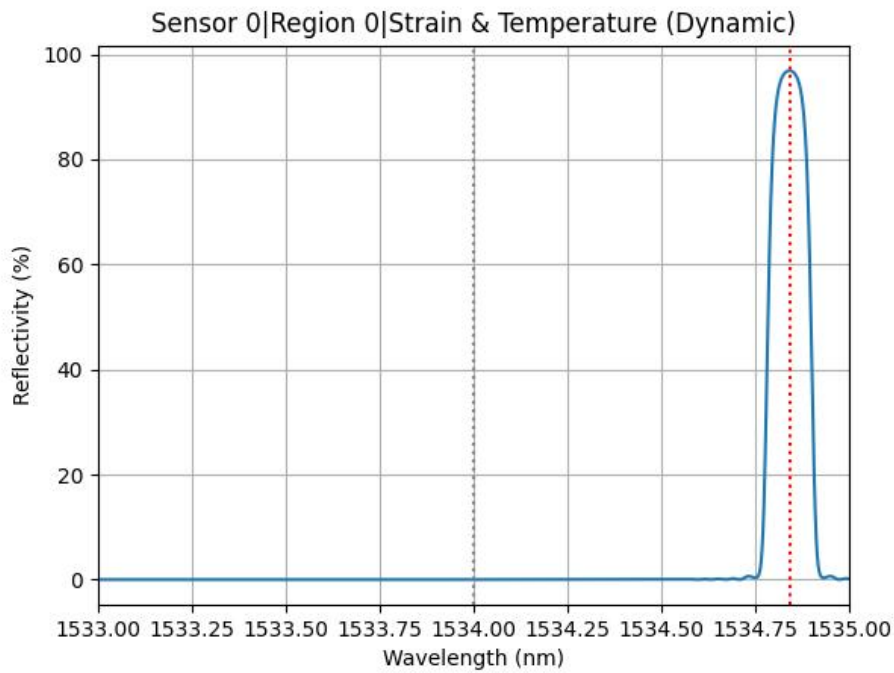


Figure 10: Temperature and strain sensor on region 0, or beam 1. The sensor is operating around a CWL of  $1538\text{nm}$ , and is shifted along the axis by a randomised liquid mass of  $16986.52\text{kg}$  at a temperature of  $42.89^\circ\text{C}$

Similar figures are recorded for the following 3 beam regions, but are not included here to avoid redundancy. Each sensor operates over the given central wavelengths established in table 1.

### 3.1.3 Simulation Summary Output

The rest of the simulation results are obtained by allowing a user to input the liquid density of the selected liquid, inputted as  $kg/m^3$ . For simulation purposes, water was used as a standard liquid type, with a liquid density of  $1000kg/m^3$ . Taking this liquid density, the following results in figure 11 were about the FBG and the tank, and were sent to the terminal.

Figure 11 displays the structured terminal output generated by the FBG simulation pipeline. The output serves as a compact and detailed report of both the raw sensor response and the interpreted physical parameters relevant to the strain, temperature, and liquid volume of the tank.

```

○○○
Enter liquid density (kg/m³): 1000
[mass_strain] mass=14904.12 kg, temp=-32.64 °C → ε=1.23e-04
=== Simulation Summary ===
(will decouple) Sensor 1 dynamic...
(will decouple) Sensor 2 static...
(will decouple) Sensor 3 dynamic...
(will decouple) Sensor 4 static...
(will decouple) Sensor 5 dynamic...
(will decouple) Sensor 6 static...
(will decouple) Sensor 7 dynamic...
(will decouple) Sensor 8 static...
Sensor 1: CWL=1534.0 nm R0=96.8% BW @ 3dB=0.116 nm R_def=96.5% εin=1.23e-04 εrec=1.23e-04 Fill=71.9% h=1.427 m Vol=14.8999 m³
Sensor 2 (T-only): CWL=1538.0 nm ΔT=100.03 °C
Sensor 3: CWL=1542.0 nm R0=96.8% BW @ 3dB=0.116 nm R_def=96.5% εin=1.23e-04 εrec=1.23e-04 Fill=71.8% h=1.424 m Vol=14.8724 m³
Sensor 4 (T-only): CWL=1546.0 nm ΔT=100.13 °C
Sensor 5: CWL=1550.0 nm R0=96.8% BW @ 3dB=0.116 nm R_def=96.5% εin=1.23e-04 εrec=1.23e-04 Fill=71.9% h=1.426 m Vol=14.8948 m³
Sensor 6 (T-only): CWL=1554.0 nm ΔT=100.24 °C
Sensor 7: CWL=1558.0 nm R0=96.8% BW @ 3dB=0.116 nm R_def=96.5% εin=1.23e-04 εrec=1.23e-04 Fill=72.0% h=1.428 m Vol=14.9169 m³
Sensor 8 (T-only): CWL=1562.0 nm ΔT=99.72 °C
=== Averages (strain+temp sensors) ===
Average input strain: 1.2336e-04
Average recovered strain: 1.2330e-04
Average recovered mass: 14896.0 kg
Average fill percent: 71.9%
Average height: 1.426 m
Average volume: 14.8960 m³

```

Figure 11: The terminal output summarising the current state of the tank and FBG given a randomised liquid mass of  $16804.17kg$  at a temperature of  $-30.88^{\circ}C$  at waters liquid density

- **Strain Calculation:** Based on the equations of beam theory 27, the strain is calculated from the applied mass.
- **Displacement Vector:** The displacement vector alternates between the computed strain values for dynamic sensors (strain + temperature) and  $\Delta T$  values for static sensors (temperature only).
- **Height Calculation:** Using the calculated strain values, the height of the liquid in the tank is estimated by inversion of the circle segment, producing values around  $1.617m$ , or approximately 81% of the full capacity of the tank.
- **Per-Sensor Temperature Reporting:** Static sensors report the measured  $\Delta T$  directly, as expected.
- **Summary statistics:** Averages across all dynamic sensors are recorded, including strain, recovered strain, mass, fill percentage, height, and liquid volume. These values provide a health snapshot of both the tank condition and the strain recovery accuracy of the system.
- **Simulation Summary Block:** Each sensor reflectivity profile is characterised by the following:
  - **CWL:** Central Bragg wavelength assigned to each FBG.

- $R_0$ : Peak reflectivity under undeformed conditions.
- $BW@2dB$ : Full-width at half-maximum (FWHM) of the spectrum, indicating sensor bandwidth.
- $R_{def}$ : Reflectivity after simulated deformation.
- $\epsilon_{in}$  &  $\epsilon_{rec}$ : The applied strain and its recovered strain from strain and temperature decoupling after FBG simulation.
- Fill, h, Vol: Liquid fill percentage, estimated height, and recovered volume.
- $\Delta T$ : Reported only for static sensors.

This set of outputs now completely verifies this simulation as an effective theoretical study of how to implement a multiplexed set of FBG sensors. From these outputs, each of the established design constraints and parameters used in the simulation can be verified with the mechanical or interrogator team, allowing for a complete communication between deformation in the physical world to readable digital data in the electrical world. Furthermore, some of these parameters can be used to influence the choice of optical fiber, as well as the technique of inscription of grating on the fiber, as explored in 4.

### 3.2 Firmware and Embedded Implementation Considerations

Although the simulation was conducted in Python, the output architecture was designed to reflect how a real FBG interrogator could interact with a C++ embedded system.

In the simulation, two Python functions, `generate_raw_sensor_output()` and `generate_displacement()` are designed to produce synthetic spectral samples and strain values that mimic real sensor readings. As this is a theoretical project and no real interrogation or hardware system is being built, this section provides a mock idea of what a real firmware implementation would look like for the FBG sensor system.

In a real system, the interrogator, or the optical front end, all static calibration data (central Bragg wavelengths, fixed point scale factors, and the thermo-optic and photoelastic constants) are stored in the MCU (RP2350[73])’s on chip flash (12 kB of program grade flash within a 16 MB device). Embedding ten 64-bit calibration values would consume only 80 bytes, providing ample room for every required constant of the program to be persistently maintained in memory.

At runtime, the MCU mechanically drives the Fabry Perot as described in section ??, where it digitally sweeps and buffers each live spectrum of 1000 photodetector samples into a `uint16t spectrum[1000]` array. A simple integer comparison loop finds the spectral reflectivity peak index, retaining the full the full 1000 point array for downstream display. After marking the spectral peak, the MCU can execute the same strain and thermal decoupling function used in the simulation, followed by the mass, volume, and height inversion mathematics run in integer or single-float calculations.

Finally, these values are serialised over the MCU’s built in UART peripheral using a simple packet format for a small header; a start byte, sensor ID, two-byte encoding for temperature and strain each, and cycle redundancy check (CRC). This is followed by the 1000 16-bit samples. The direct UART peripheral of the MCU streams the approximately 2 kB of data directly via a USB-host port on the operator’s laptop (no USB bridge chip is needed), so each firmware update or configuration change propagates seamlessly. The on device application receives each 1000 point trace and renders it in real time, then applying the simulations `decouple_temperature_strain()` function logic in floating-point to extract the change in temperature  $\Delta T$  and the applied strain  $\epsilon$ , mathematically converting strain to a liquid mass present within the tank, which will correspond to a liquid fill % and finally obtaining an active liquid height, while displaying reflectivity spectrum plot on a user dashboard.

## 4 Fiber Bragg Grating Fabrication

With the complete modeling and simulation of the FBG, the next step to bring this design to a real world application would be to fabricate a real FBG. To do this, an optical fiber with the desired phot-elastic coefficients used in the simulation needs to be selected to begin the fabrication process. Furthermore, selection of a valid inscription method is dependent on the desired grating length and apodization profile.

## 4.1 Inscription Methods

Before selecting the fiber, the different methods for inscribing the fiber will be explored. FBG fabrication involves creating a periodic modulation of the refractive index within the core of a selected fiber optic cable. The periodic structure behaves as a selective reflector of particular wavelengths, forming a foundation for Bragg wavelength specific reflection capabilities of the FBG sensor. For inscription, some choice of laser source can be used, with selection again depending on the photosensitive fiber option, grating length and periodicity as well as the intended application [8].

Inscription methods at their core involve inscribing periodic index modulations on the core of the fiber as the grating. These methods can typically fall into two generalised categories, holographic interferometre and noninterferometric techniques.

### 4.1.1 Holographic Interferometry

The holographic inscription uses two laser beams to create an interference pattern that produces the periodic index modulation, which in the simulation is set to  $\Delta n_{eff} = 1 \times 10^{-4}$  2.4.1. The laser beams typically consist of two UV emission spectrum, which are split and directed by mirrors to interfere onto the fiber at a specific angle. When two of these beams constructively interfere, this interference results in a sufficiently high intensity that can permanently alter the effective refractive index of the fibers core, noting that the fiber core must meet a minimum photosensitivity requirement for this inscription to work.

The holographic method enables a Bragg wavelength, or grating periodicity to be chosen as a result of the wavelength of the UV spectrum emission as:

$$\lambda_B = \frac{n_{eff}\lambda_{UV}}{n_{UV}\sin(\frac{\theta}{2})} \quad (36)$$

[8]

Where,

- $\lambda_B$  is the Bragg wavelength
- $n_{eff}$  is the effective mode index of the fiber
- $n_{UV}$  is the refractive index of silica in the UV
- $\lambda_{UV}$  is the wavelength of the laser being used to write the grating
- $\theta$  is the angle that each of the interfering beams meet at  $\angle L_1 L_2$

The holographic masking technique is effective for short grating lengths  $L$ . However, it is unsuitable for this simulation which uses a long grating length of 200 mm, marking this technique as not useful.

### 4.1.2 Phase Mask Method

The noninterferometre's adoption of the phase mask component offered a new and easier way of inscribing the FBG. A phase mask is used in transmission as relief grating etched in to a silica plate. This silica plate is the transmitter for the laser, where the etchings are specifically designed for a particular periodicity and depth in the plate. The inscribing is established by the "diffraction of an incident UV into several orders,  $m = 0, \pm 1, \pm 2 \dots$ " This can be expressed in the following figure 12:

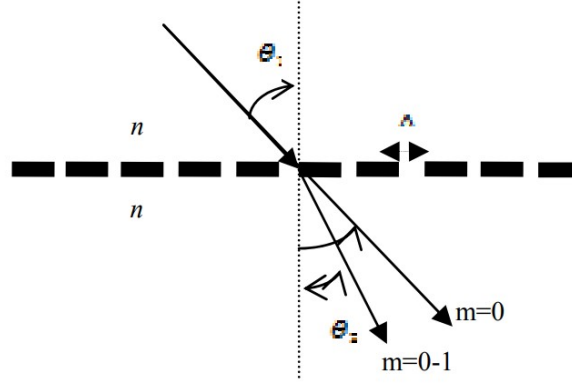


Figure 12: Diffraction of an incident beam from a phase mask portrayed schematically. [18]

The equation to satisfy figure 12 is:

$$\Lambda_{pm} = \frac{m\lambda_{UV}}{\sin\frac{\theta_m}{2} - \sin\theta_i} \quad (37)$$

Where,

- $\Lambda_{pm}$  is the grating etched into the phase mask
- $\frac{\theta_m}{2}$  is the diffraction order angle
- $\lambda_{UV}$  is the wavelength
- $\theta_i$  is the angle that the UV emission is incident at

Alternatively, when the laser is emitted at a normal incident to the phase mask, where  $\theta_i = 0$ , the diffracted radiation spectrum is split into 3 "even" orders,  $m = 0$  and  $m \pm 1$  orders. At the fiber, this produces an interference pattern where the two  $m \pm 1$  emissions are positioned back together by parallel mirrors. This diffraction is shown in figure 13.

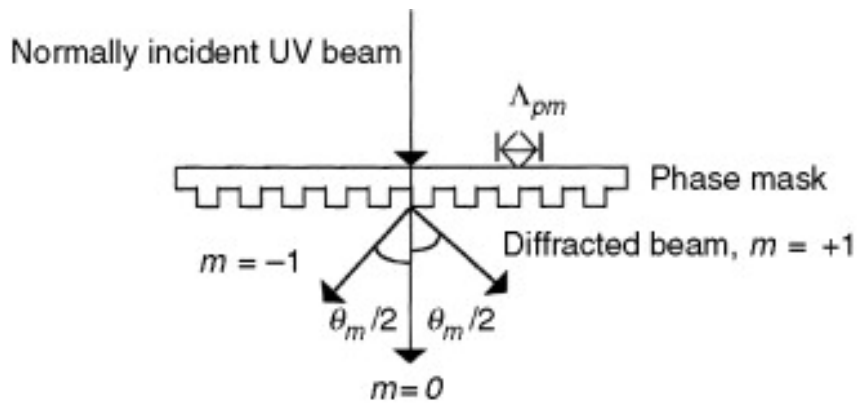


Figure 13: Diffraction of a normally incident ( $\theta_i = 0$ ), separating into two emission beams of orders  $m \pm 1$ . The left over radiation departs the mask separately as a zero order spectrum  $m = 0$ . [8]

The relationship between the angle of diffraction and grating period for this mask is as follows:

$$\Lambda_g = \frac{\lambda_{UV}}{2\sin(\frac{\theta_m}{2})} = \frac{\Lambda_{pm}}{2} \quad (38)$$

[8]



The Bragg condition<sup>1</sup> is essential for understanding the behavior of an FBG, and as such the Bragg wavelength is a key determining factor for forming the grating Length. Relating the Bragg wavelength into 38 produces:

$$\Lambda_g = \frac{N\lambda_{Bragg}}{2n_{eff}} = \frac{\Lambda_{pm}}{2} \quad (39)$$

These equations are relevant as they build towards a tool that can be used to inscribe multiple different gratings, each defined by their own selection of central Bragg wavelengths that they need to operate over as shown in table 1. These central wavelengths are a primary definer for which FBG fabrication technique is used, and how to appropriately create the grating for each sensor.

Combining these equations, a function using the angle between interference beams can be created to represent the shifting Bragg wavelength. As such, equations 37 and 38 are substituted into equation 36, differentiating with respect to the phase angle for:

$$\frac{\Delta\lambda}{\lambda_{Bragg}} = -\frac{\Delta\theta}{2} \cot\frac{\theta}{2} \quad (40)$$

[8]

The unfortunate truth for this type of phase mask however, is that it requires significant stitching between fabricated pieces that are inscribed in small fields. Leading to speculative reports of this technique being able to produce a grating length of around 120 mm before the grating succumbs to "random variations in the individual periods of the grating" [8]. This 120 mm length is still excessively shorter than the FBG length used in the simulation of 200 mm. Put shortly, holographic techniques struggle to produce long grating lengths, but the technique of being designed to suit the required Bragg length of the grating is a start of particular importance.

#### 4.1.3 Multiple Printing in Fiber (MPF)

Finding a sufficient technique for an ultra long grating of 200 mm is not straight forward. The phase mask technique explored above could be used repetitively but it will encounter the issues of variable periods in the grating.

A well defined system for writing an ultra long fiber comes in the form of the multiple printing in fiber (MPF) technique from the Raman Kashyap book [8]. Here, the grating is written as a series of discrete segments that are incrementally shifting the optical fiber underneath a fixed phase mask, alternatively, the UV emission can be moved along the fiber for the same effect. The divided segments are exposed to a high precision beam, with resulting overlaps producing a continuous grating structure. Sections completed in a modular fashion now have the potential to function as one longer grating length, well beyond the depth of field limitation that was presented before by the simple phase mask interference pattern. Doing this allows for control of grating length, index modulation, and apodization profile.

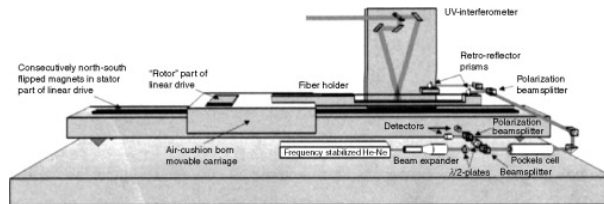


Figure 14: Multiple printing in fiber device, capable of writing grating lengths of 200 mm, suitable for previous simulation setup.

[8]

For this FBG design, relatively maximum reflectivity was sought in the simulation. The MPF technique can adjust the overlap and exposure parameters between the printed sections, the grating's side lobe levels for apodization and fine tune the bandwidth of the grating. On these alone, the MPF seems to be a significant choice for fabricating the ultra long grating demonstrated in the simulation.

However, MPF does retain some of the superseding limitations. MPF requires extremely precise mechanical and optical control. Even the smallest misalignment during translation from mask to fiber, or inconsistencies in the UV exposure of the prolonged length of the grating can cause intolerable phase discontinuities, introducing spectral defects including reflection ripples and unwanted side lobes. The technique is also highly sensitive to vibration, needing obtusely stabilised and costly setups to mitigate external disturbances. Furthermore, similarly to the progressive stitching of the longer phase mask gratings, each additional section increases further risk of cumulative error, reducing reliability and reproducibility of the grating. For a optical fiber with eight ultra long gratings, this method is incredibly labour intensive and is not well suited to industrial production for many tanks, regardless of ability to customize the profile of the grating itself.

#### 4.1.4 Realising the Grating Length

While a 200 mm grating was originally modeled for simulation fidelity, practical constraints in available fabrication methods meant that this grating length needed to be revised.

By retuning factors in the simulation, such as grating length down to 120 mm, the system retains a peak spectral reflection of 79.9% and a bandwidth of 0.134 nm represented in figure 15, highlighting it can potentially go even further depending on the limits of the interrogators ability sufficiently obtain any meaningful data from reflected signal.

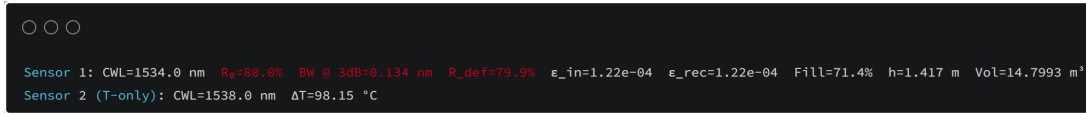


Figure 15: Simulation output of 120 mm long Grating

Given this information, a decision can be made to balance between cost of money, time and accuracy in fabrication, versus the ability to relay constructive information about the tank via spectroscopy.

From spectroscopy, the minimum reflectivity that can carry a meaningful signal can be as small as 60%. The simulation can be refined to the previous slated 120 mm length.

As a result, a sufficient FBG sensing system for measuring liquid height and monitoring SHM can be achieved with a far shorter grating length of 120 mm, as opposed to the original 200 mm. To fabricate this, the phase mask technique of stitched together segments is to be employed, providing Gaussian apodization, a reliable grating profile while being scalable to many tanks.

Cost of inscription is hard to deduce without get real quotes, and writing on to fiber cores is not a typically spoken about item in terms of costs. A conservative assumption could put single grating inscription at up to £150, which could place the total cost of eight FBG's for one tank at £1200. This is assumedly far cheaper than setting up an in house fabrication unit, which would likely take a large amount of time to see any sort of return on investment (ROI).

#### 4.1.5 Pre-processing of Fiber Core before Fabrication

Before the grating can be inscribed, the fiber core itself must be meticulously prepared. Raman Kashyap [8] writes about the significance of this preparation phase, emphasising how the fiber's condition directly influences the efficiency and reliability of the grating inscription process. In particular, for applications involving strain and temperature such as this project, there is a requirement for an optical fiber core with a correct effective refractive index  $\Delta N_{eff}$ , of a propagating mode that is sensitive to strain and temperature. The fiber core must be inscribed with this sensitivity taken into account, otherwise misaligned sensitivities will result in an inconsistent Bragg wavelength during measurement.

To prevent this, the fiber core can be pre strained or pre heated during the writing process. For example, if the fiber is preheated to a writing temperature  $T_w$  and later used at a lower operational temperature  $T_f$ , the Bragg wavelength will shift based on both the thermal expansion and the thermo-optic effect. Thus, the Bragg wavelength after fabrication is given by:

$$\lambda_B = 2L_g(1 + \alpha(T_f - T_w))n_{eff} + \frac{dn_{eff}}{dT}(T_f - T_w) \quad (41)$$

The expression is intended to highlight how the Bragg wavelength is dependent on both material expansion  $\alpha$  and index change  $\frac{dn_{eff}}{dT}$ . simplifying this further, the shift in Bragg wavelength is:

$$\Delta\lambda_B \approx 2L_g \frac{dn_0}{dT} (T_f - T_w) \quad (42)$$

Where  $\frac{dn_0}{dT}$  incorporates both thermal expansion and the refractive index change. [8]

Likewise, prestraining the fiber alters the final grating structure. Once relaxed, the period of the grating and local effective index adjust accordingly, leading to a chirped grating, even if during inscription a uniform period was written. Chirping arises due to the uneven strain relief along the fiber, influencing both the grating's reflection profile and sensitivity characteristics.

These preconditioning technicalities are essential for targeting the correct Bragg wavelength but also for engineering desirable spectral features such as bandwidth. In this tank sensing system, the strain and temperature sensors require precise Bragg alignment, which is critical to correctly decoupling the two parameters in real time. As such, a pre conditioned fiber will be inscribed using a stitched phase mask along a 120 mm, apodized grating length.

## 4.2 Fiber Optic Cable Selection

The optical fiber cable that is utilised for this FBG system must be compatible with the selected writing method, support the desired reflectivity and grating length, and maintain stability under the expected environmental conditions presented by the tank and its surrounding area. Given the use of a UV laser, phase mask inscription method and a set of target Bragg wavelengths around 1500nm as shown in table 1, a standard single-mode silica fiber with a core diameter of 8 - 9  $\mu\text{m}$  and a cladding diameter of 125  $\mu\text{m}$  is applicable.

This configuration offers a balance between photosensitivity, structural flexibility and reliability, as well as compatibility with phase mask inscription. The simulation used a refractive index modulation depth of  $\Delta n = 1 \times 10^{-4}$ , aligning with the capabilities of germanium-doped core fibers under UV radiation exposure.

For fabrication, fibers with pure silica cores and polyamide acrylate coatings are commercially available from fiber vendors such as Fibercore and Exail. These fibers are designed for long term performance under strain and moderate thermal variations, specifically for the application of structural health monitoring, and are compared in table 4.2.

Table 2: Comparison of Selected Optical Fibers for FBG Inscription

Parametre	Fibercore SM1500(9/125)HT	Exail IXF-PMF-1550-125-P-012
Core Diameter ( $\mu\text{m}$ )	9	8.5
Cladding Diameter ( $\mu\text{m}$ )	$125 \pm 1$	$125 \pm 1$
Numerical Aperture (NA)	0.13–0.15	$0.12 \pm 0.01$
Mode Field Diameter ( $\mu\text{m}$ )	8.5–9.9 1550 nm	$10.5 \pm 0.5$ 1550 nm
Attenuation (dB/km)	$\leq .35$ 1550 nm	0.5 1550 nm
Coating Type	High-temperature acrylate	Dual-layer UV acrylate
Operating Temperature ( $^{\circ}\text{C}$ )	-55 to +150	-40 to +85
Photosensitivity	High (suitable for FBG inscription without hydrogen loading)	High (suitable for UV inscription)
Polarization Maintaining	No	Yes
Applications	Distributed sensing, structural health monitoring	Fiber optic sensors, gyroscopes, instrumentation
Manufacturer	Fibercore (Humanetics Group)	Exail
Reference	[19]Fibercore Datasheet	[20]Exail Datasheet
Cost Estimate	Contact for pricing *	€13.00/m (min. 10 m)

Given the performance needs of the designed FBG sensing system, such as high photosensitivity as stated in section 4.1.2, thermal stability, and a standard single-mode configuration (9/125 $\mu\text{m}$  as required to ensure narrow band reflectivity and optimal Bragg wavelength stability as discussed in section 1.2.1,

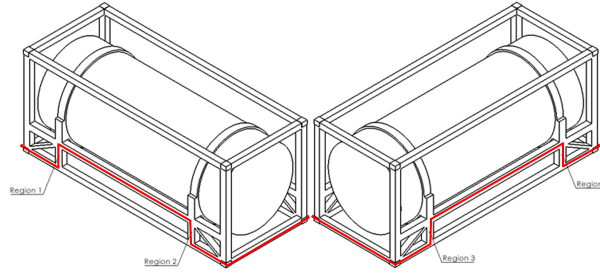


Figure 16: Optical Fiber Multiplexed Path Around Tank Frame

the Fibercore SM1500(9/125)HT emerges as the optimal choice. It meets all the design criteria simulated in section 2.4.1, including the required refractive index, coating durability for survival under harsh or corrosive conditions, and minimal attenuation. Unlike the Exail fiber, which is tailored for a different type of precise instrumentation, the Fibercore fiber avoids unnecessary complexity while offering a wider operating temperature range ( $-55^{\circ}\text{C}$  to  $+150^{\circ}\text{C}$ ), for critical long term deployment in variable environments to measure strain and liquid level while reporting on the structural health of the constituent tank.

While the official pricing is not listed directly on the Fibercore website[19], similar high temperature and single mode fibers such as the Newport F-SM 1500-9/125-P[21] typically retail at £8.00 metre, versus the excluded Exail IXF-PMF-1550-125-P-012 which comes in at €13.00 metre with a minimum spend purchase of 10 m or €10.50 metre which a minimum purchase of 100 metres, those are respectively £11.00 metre and £8.88 metre. Both fiber options average at around £9.00 metre, this will be the extrapolated cost of the chosen Fibercore fiber, avoiding seeking a quote from the manufacturer.

The length of fiber required is such that a single multiplexed fiber can entail the entire frame structure, while the routing of the fiber across the frame adequately attaches to the given sensor locations established in ???. To sufficiently reach around each sensor location, the cable wraps around the frame twice as shown in figure ??.

The cable, highlighted by the red line in figure 16, is wrapped around the frame twice to enable the strain and temperature decoupling discussed in section 2.5, where two sensors are required for a single beam location in order to separate thermal expansion effects from strain deformation effects on a strain sensitive grating.

Thus, using the dimensions of the frame from figure ??, where the sensor is located vertically up the 270.00 mm high beam, the beams are separated by 3796.00 mm along the length of the tank and 2432.40 mm along the width of the tank, and the distance between the beam and the edge of the frame is 950 mm.

Therefore, following the fiber optic path presented in 16, and removing the final width after the 8th sensor, the required length can be defined as:

$$\text{Cable Length (mm)} = 4 [2(270) + 3796] + 3 [2(950) + 2432.4] \quad (43)$$

From this, the required minimum cable length is 30 341.2 mm, or 30.34 m. This is a minimum as the attached cable will require loosened connections, avoiding right angles or unnecessary damaging strain to the cable itself (note, this is completely separate to the recorded stress of the tank, and is pertaining to the health of the fiber optic cable itself). Testing splices are also necessary and general FBG fabrication will include off cuttings as any manufacturing process does. As a result of these, a modest and safe 3.00 m is added to this final total, meaning that each tank will have an allocated 33.00 m, rounding to the nearest metre.

At a length of 33.00 m, the projected pricing of the Fibercore fiber will come to £297 per tank. Or, given that the FBG sensor systems will be produced for a number of ISO tanks at once, utilising bulk buying such as the Exail IXF-PMF-1550-125-P-012 £8.88 metre for 100 m, buying a km of fiber optic cable could provide ample cabling for up to 35 Tanks with FBG enabled strain sensing, coming at a price of ≈£8,888.

### 4.3 Epoxy Adhesive Selection

In essence, the fiber optic cable only needs to be completely attached to the frame structure where the grating is used as a strain sensor, or around the grating the acts as the thermal compensator sensor. Otherwise, it is preferable that the cable follow the length of frame tightly so as to reduce cable waste, but the attachment for anywhere where this is no grating is trivial. The strain sensor must be completely attached to the frame so that it can experience liquid induced strain at the same rate that the tank tank does, but while being entirely fixed in place it must still maintain its ability to deform under strain and thermal effects. Conversely, the thermal only FBG has to be fixed in place at the exact same location as the strain sensor while being in parallel so as to experience identical thermal effects as the strain sensor for calibration. This means the thermal only sensor needs to be bonded to the tank so that it does not move from its assigned location, but with enough slack, and far enough away from the grating so as to not experience any strain induced deformation.

As such, the selected adhesive must ensure correct translation of tank strain onto the FBG and be able to secure the sensor without damaging the cladding while accommodating thermal expansion without delamination. The bond strength must be able to withstand the highest strain that the liquid can induce on the tank. Quickly utilising the designed FBG simulation in section 5, testing for a full tank of Sulfuric acid, a highly dense liquid  $1.83 \text{ g/cm}^3$  liquid density, the recorded strain on the tank is  $3.1194 \times 10^{-4}$ , therefore as an example, the bonding strength of the adhesive must be able to exceed this strain presented. Using Hooke's, the minimum required bond strength for the adhesive can be determined by:

$$\text{Stress } \sigma = E \times \epsilon \quad (44)$$

Using the Young's modulus of the frame from table ?? as 210 GPa, the stress from sulfuric acid is 65.51 MPa. This would come as the theoretical tensile strength if the full strain was experienced through the bonded Corten B steel. However, the adhesive typically does not need to withstand the entire micro stress applied to the substrate, where only 82% of the strain is transferred over an adhesive length of 12 nm [22]. Even still, a stress of 53.71 MPa remains significantly high, but this number only represents the theoretical stress required to perfectly match the frames strain over the bonded length as adhesives do not experience uniform stress along their length. It can be noted that, the actual strain transmitted is firstly lower due to the compliant interface of the epoxy and the adhesive loading is distributed and not at a concentrated point. In practice, adhesives in FBG systems do not fail even the strain transfer implies  $\pm 30 \text{ MPa}$  equivalent strength [23].

As such, an epoxy can be selected with bond strength that is seemingly far less than the theoretical max stress, as presented by an extremely dense liquid not often transported.

The effective adhesive choice is Epoxy EPO-TEK 353ND [24]. A two component, high temperature epoxy adhesive with high strength, thermal stability and compatibility with fiber optic applications. It is specifically reliable in semiconductor and medical applications.

Table 3: Key Properties of EPO-TEK 353ND Relevant to FBG Applications

Property	Description
Bond Strength	High shear strength ensures reliable strain transfer without damaging the fiber; exceeds 20 MPa.
Thermal Stability	Operates continuously up to 250°C, withstands intermittent exposure up to 350°C.
Chemical Resistance	Resists degradation from common solvents and industrial chemicals.

Thorlabs sells EPO-TEK 353ND[25] as a high temperature and low CTE epoxy under part number 353NDPK, which comes with 4g Packets, 10 per pack at £72.46. An extremely small amount of epoxy will need to be applied by syringe per 120 mm sensor, where only 4 sensors have the full length attached to the frame. However, given the fiber will need to be attached to the frame at other points along the frame reduce cable waste and reduce chance of loose fiber damage. As such, the single 353NDPK purchase could suffice for well over 35 tanks, where only on a fraction of a gram of epoxy is required for each sensor attachment.

#### 4.4 Attaching the FBG to the Tank

Further information that can be derived from figures 16 and ?? as well as the equation 43 are the exact positions along the length of the fiber where each grating needs to be inscribed. Relating this information with central wavelengths in 1, each specific sensor type and location can be prescribed to a location the fiber for FBG fabrication and inscription to commence. The FBG sensor type and its respective location are shown in table ??.

Table 4: Sensor Type, Bragg Wavelength and Sensor Location Along Fiber for Comprehensive FBG Fabrication

Beam	1		2		3		4	
Sensor Index	1	2	3	4	5	6	7	8
Strain + Temp ( $nm$ )	1534	-	1542	-	1550	-	1558	-
Temp Only ( $nm$ )	-	1538	-	1546	-	1554	-	1562
Sensor Location (mm)	75	17411.8	4141	21477.8	8743.4	26080.2	12809.4	30146.2

Each beam region in table 4 will contain its constituent sensor pair, attached to the beam by an epoxy resin as shown in figure 17.

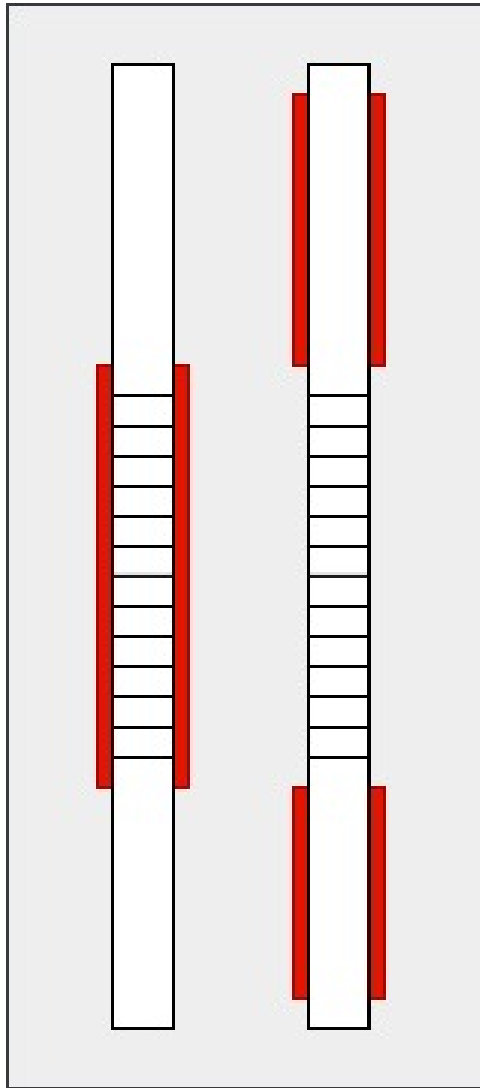


Figure 17: Diagram of FBG attached to Beam on Frame Structure by Appropriately Placed Epoxy Resin

In figure 17, the region regions represent application of epoxy resin, with the horizontal line pattern representing the grating in the fiber which is represented by longer vertical rectangle, with the grey background being the beam. One sensor is attached to the beam across the grating, experiencing both strain and thermal deformation, and the other is only held in place outside of the grating to exclusively feel the surrounding thermal effects. This figure is not to scale.

#### 4.5 Complete Attachment of Grating Inscribed Fiber Optic Cable for Interrogation

Given the complete modeling of the propagating wavemodes within the core of a select optical fiber, techniques have been explored to inscribe a grating onto the core of the fiber so that external deformations by an induced strain or thermal affects can effectively manipulate a wavelength to be read electronically at an interrogator. This FBG sensing system was design backwards, using a thorough mathematical modeling of the counter propagating light in a fiber to create a digital simulation of the FBG's that would be attached to the tank. The simulation aided the physical design of the FBG, being used to realise the parameters that would allow for a real translation of the strain experienced on a tank frame to a readable digital value. The simulation was further used as a twin to what would be a real firmware implementation, where the recorded reflectivity spectrum from an FBG can be used to calculate a strain and in turn deduce the volume of liquid in a tank, and thus the liquid height in a tank, replacing traditional methods of dipstick measurements, or other sensors that are ill suited to the environmental factors that the ISO container experiences. Furthermore, this FBG design uses its strain sensitive abilities to establish a working structural health monitoring system as discussed in section ??, where strain measured over time is used as indicator of the health of the tank.

This concludes the FBG design established by sections 1, 5, 3 and 4, as such, the inscribed FBG is ready to be effectively integrated by the spectrometer for the ready of the reflected central Bragg wavelength.